



Bulk-to-nano regulation of layered metal oxide gears H_2O_2 activation pathway for its stoichiometric utilization in selective oxidation reaction

Guohan Sun^a, Molly Meng-Jung Li^b, Keizo Nakagawa^c, Guangchao Li^b, Tai-Sing Wu^d, Yung-Kang Peng^{a,e,*}

^a Department of Chemistry, City University of Hong Kong, Hong Kong

^b Department of Applied Physics, Hong Kong Polytechnic University, Hong Kong

^c Research Center for Membrane and Film Technology, Graduate School of Science, Technology and Innovation, Kobe University, Kobe 657-8501, Japan

^d National Synchrotron Radiation Research Centre, Hsinchu 30076, Taiwan

^e City University of Hong Kong Shenzhen Research Institute, Shenzhen 518057, China

ARTICLE INFO

Keywords:

H_2O_2 activation pathway
Surface chemistry
Brønsted and Lewis acids
Selective oxidation
Niobates

ABSTRACT

H_2O_2 has been widely used as a green oxidant in many heterogeneous reactions. However, its disproportionation accelerated by either Brønsted acid (BA) or redox metal sites often results in low H_2O_2 utilization. Given this, metals less able to redox have been used because the formation of surface metal-peroxo species exhibits a certain degree of selectivity towards substrates. However, those catalysts often bear BA sites on their surface for charge balance, making it imperative to study H_2O_2 activation pathway in the presence of both sites. Herein, layered HfNb_3O_8 with structurally preserved BA sites was used for this purpose. We found that the exposure of Nb sites via bulk-to-nano regulation of this material hinders H_2O_2 disproportionation promoted by BA sites. Among various Nb-peroxo species, its bidentate configuration formed on highly distorted NbO_x was found to provide the best reactivity in alkene epoxidation with a near stoichiometric H_2O_2 utilization.

1. Introduction

Hydrogen peroxide (H_2O_2) is an important green oxidant for a wide range of catalytic reactions with water and oxygen as the by-products [1–4]. Although the development of solid catalysts for H_2O_2 synthesis has gained much attention recently [5–7], optimizing its utilization in a given reaction is equally important but less studied. The activation of H_2O_2 is believed to closely associate with surface features on solid catalysts such as Brønsted acid (BA) and Lewis acid (LA) sites. BA sites could facilitate the disproportionation of H_2O_2 ($2 \text{H}_2\text{O}_2 \rightarrow 2 \text{H}_2\text{O} + \text{O}_2$) via a radical-mediated pathway. As shown in Scheme 1a, the reduction of H_2O_2 (to H_2O) first generates OH radicals (Eq. (1)), which later oxidize another H_2O_2 producing HO_2 radicals (Eq. (2)). The whole cycle is completed by the oxidation of HO_2 radicals (Eq. (3)) by the H_2O_2 in Eq. (1). Radicals produced in this pathway thus accelerate the disproportionation of H_2O_2 resulting in its low utilization. In addition to BA sites, transition metal-associated LA sites with good electron transfer property (e.g., oxides of Mn, Fe, Cu, Ce, etc.) decomposes H_2O_2 via a well-known Fenton process (Scheme 1b) [8–14]. The redox between M^{n+} (oxidation) and H_2O_2 (reduction) firstly generates OH radicals (step

(a)). Those OH radicals in the reaction solution oxidize not only target substrates (step (b)) but also free H_2O_2 to produce HO_2 radicals (step (c)) for M^{n+} regeneration (step (d)). Many reducible metal oxides have been reported so far to convert H_2O_2 to radicals for applications ranging from biosensing and biomedicine to wastewater treatment [15]. By knowing that step (a) is the rate-limiting step (i.e., the redox reaction between M^{n+} and H_2O_2), we recently boosted this conversion on pristine CeO_2 (up to 20 times) by tuning the local structure and chemical state of surface Ce species [16,17].

Despite this radical-mediated pathway being associated with a wide range of applications, the oxidation of not only substrates but free H_2O_2 in the solution also results in poor H_2O_2 utilization. Literature has thus suggested the use of metal cations less able to redox (e.g., Zr, Al, Ti, Nb in alkene epoxidation [18–26]) because the formation of surface metal-peroxo species could exhibit a certain degree of selectivity towards substrates giving an improved H_2O_2 utilization (Scheme 1c). The selectivity and reactivity of metal-peroxo species are believed to be further optimized by tuning the local structure and chemical state of LA sites as we did previously for CeO_2 [16,17]. Since those metal oxides often bear BA sites on surface for charge balance (e.g., zeolites), the

* Corresponding author at: Department of Chemistry, City University of Hong Kong, Hong Kong.

E-mail address: ykpeng@cityu.edu.hk (Y.-K. Peng).

<https://doi.org/10.1016/j.apcatb.2022.121461>

Received 2 March 2022; Received in revised form 9 April 2022; Accepted 26 April 2022

Available online 4 May 2022

0926-3373/© 2022 Elsevier B.V. All rights reserved.

understanding of the interplay between both acid sites and H_2O_2 is thus critical for optimizing its utilization. This point is, however, less studied presumably due to the unsatisfactory information provided by conventional surface techniques (vide infra) [27,28].

Herein, HNb_3O_8 consisting of edge-shared NbO_6 layers interconnected by bridged protons (Scheme 1d) is adopted for this purpose. As expected, BA sites on the terminal surfaces of bulk HNb_3O_8 (b- HNb_3O_8) facilitate H_2O_2 disproportionation via a radical-mediated pathway, leading to low H_2O_2 utilization and radical-mediated products in alkene oxidation. As revealed by nuclear magnetic resonance (NMR) and X-ray absorption (XAS), the reduction of layers of this material to few (f- HNb_3O_8) and single (s- HNb_3O_8) layer exposes Nb sites with distinct LA strength depending on the distortion of surface NbO_x units. The Nb-OOH species formed on f- HNb_3O_8 was found to promote alkene epoxidation and at the same time hinder H_2O_2 disproportionation. Surprisingly, the latter reaction was completely quenched on s- HNb_3O_8 when BA sites involve in the protonation of Nb- $\eta_2\text{-O}_2$ species. This, together with its high turnover frequency (TOF) towards alkene epoxidation, makes s- HNb_3O_8 a promising catalyst with a near stoichiometric H_2O_2 utilization in this model reaction. This work not only demonstrates a facile method to steer the activation pathway of H_2O_2 (i.e., bulk-to-nano material engineering) but provides an insight into their interplay with BA and LA sites on catalysts' surface.

2. Experimental section

2.1. Synthesis of HNb_3O_8 samples

Bulk HNb_3O_8 (b- HNb_3O_8) can be obtained by cation exchange of layered KNb_3O_8 precursor [29]. For the preparation of KNb_3O_8 , 0.01 mol K_2CO_3 and 0.029 mol bulk Nb_2O_5 (Sigma-Aldrich) were mixed and then calcined at 873 K for 2 h and 1173 K for 3 h. The resulting material (i.e., KNb_3O_8) was then immersed in 150 mL 6.0 M HCl for 72 h at room temperature followed by a thorough wash by distilled water. The product, b- HNb_3O_8 , can be obtained after calcination at 423 K for 3 h. Few-layer HNb_3O_8 (f- HNb_3O_8) and single-layer HNb_3O_8 (s- HNb_3O_8) were synthesized by a bottom-up hydrothermal method [29]. Typically, 6.25 mmol $\text{Nb}(\text{OEt})_5$ was dissolved in 25 mL ammonia solution (30%). Note that 25 mmol triethanolamine (TEOA) was additionally added for the preparation of s- HNb_3O_8 . The mixture was then transferred into a 45 mL of Teflon autoclave and aged for 24 h at 433 K. The precipitate was then washed with ethanol and soaked in 1.0 M HNO_3 solution for

5 h. The resulting product was further washed by distilled water before use. To replace BA sites on s- HNb_3O_8 with Na^+ , 0.05 g catalyst was dispersed in 10 mL of 0.2 M NaCl solution maintained at pH = 5.5–5.8 by adding 0.05 M NaOH solution. After 24 h stirring, the sample was collected by centrifugation, washed with distilled water and dried at 373 K for 12 h.

2.2. X-ray diffraction (XRD) and nitrogen adsorption/desorption

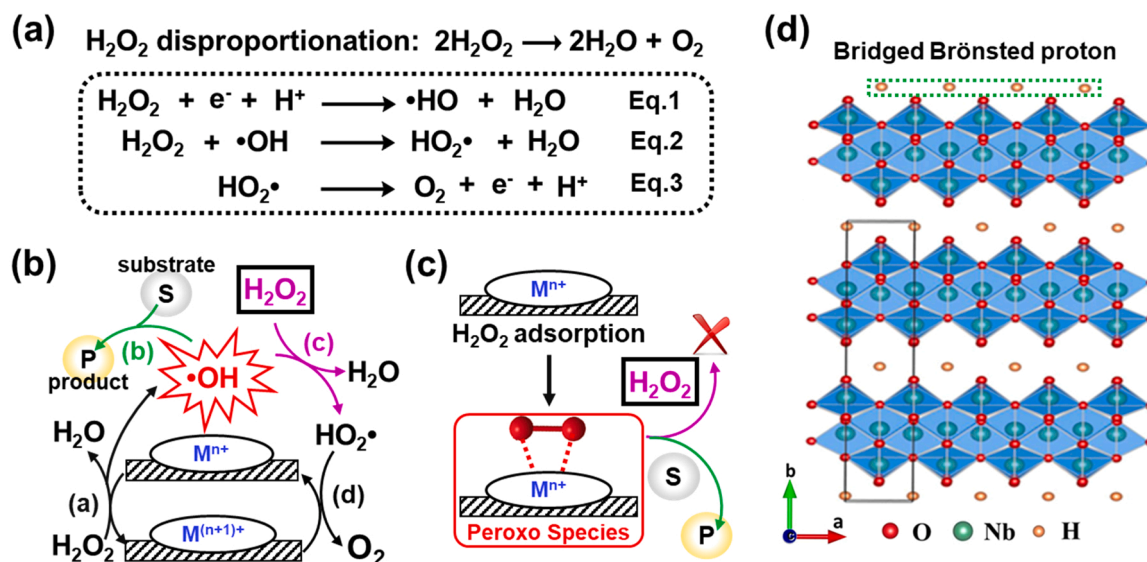
Crystalline phases of the niobium oxides were identified by powder XRD (D2 PHASER 2nd gen, 178 Bruker) with monochromatized $\text{Cu K}\alpha$ radiation. For nitrogen adsorption/desorption measurement, specific surface areas were estimated from the corresponding adsorption/desorption isotherms at 77 K with a conventional BET nitrogen adsorption apparatus (BELSORP 28SA, MicrotracBEL Corp.).

2.3. Pyridine-infrared spectroscopy (pyridine-IR)

In a typical procedure, 10 mg HNb_3O_8 sample was pre-treated at 393 K for 1 h before pyridine adsorption. The pre-treated sample was then mixed with 3 mL pyridine and stirred for 1 h at the room temperature. To remove free pyridine, this mixture was then treated at 453 K under vacuum for 1 h. IR spectroscopy was recorded on a Perkin Elmer Spectrum 100 using attenuated total reflectance (ATR) method.

2.4. Trimethylphosphine (TMP) ^{31}P NMR

50 mg HNb_3O_8 sample was pre-treated at 393 K for 1 h under vacuum before TMP loading at room temperature. TMP can be vaporized under vacuum and adsorbed on sample surface in a separated vial connecting by Schlenk line. When the pressure in both vials reaches a plateau, suggesting that an equilibrium state has been achieved between the gaseous TMP and the TMP-adsorbed sample. Excess TMP in the sample vial can be removed by a gentle vacuum treatment. The TMP-adsorbed sample was then transferred to 4 mm ZrO_2 rotor under nitrogen protection for NMR measurement. Solid-state magic angle spinning (MAS) NMR measurements were carried out using a Bruker Avance III 400WB spectrometer at room temperature. To remove the effect of proton spins on quantitative ^{31}P spectra, the high-power decoupling was used in this study with decoupling radiofrequency at 59 kHz. 30° pulse with 1.20 μs width and 15 s delay time was used. The MAS spinning frequency was 10 kHz. The ^{31}P chemical shifts were reported relative to



Scheme 1. Schematic illustration of H_2O_2 activation pathway associated with (a) Brønsted protons, Lewis metal sites with (b) good electron transfer property and (c) less redox ability. (d) Crystal structure of layered HNb_3O_8 .

85% aqueous solution of H_3PO_4 . The quantitative information of adsorbed TMP molecules was obtained based on the calibration line established by standard samples with known phosphorus concentrations.

2.5. X-ray absorption (XAS)

Measurements of the Nb K-edge X-ray near edge structure (XANES) performed at beamline BL07A of the Taiwan light source at the National Synchrotron Radiation Center. The corresponding local atomic structures were studied using the extended X-ray absorption fine structure (EXAFS) technique.

2.6. Electron paramagnetic resonance (EPR)

EPR spectra were recorded with an ADANI SpinscanX spectrometer, operating at 100 kHz field modulation using the 150 ut modulation amplitude. 5,5-dimethyl-1-pyrroline N-oxide (DMPO) was chosen as the spin trap. For the trapping of OH radicals, typically, 10 mg of the catalyst and 2 μL DMPO were dispersed in 1 mL DI water. The reaction can be initiated by the addition of 500 μL H_2O_2 aqueous solution (30%) at 333 K. Small aliquots were sampled at a given time point (5 min, 15 min and 30 min) followed by catalyst removal via centrifugation (12,000 rpm/5 min). The supernatant was then transferred to a quartz capillary, and the EPR spectra were recorded at room temperature. Methanol was using instead of DI water for the trapping of HO_2 radicals.

2.7. H_2O_2 disproportionation

The disproportionation of H_2O_2 over HNb_3O_8 samples was studied at 333 K under the same condition described in catalytic testing. While the decomposition of H_2O_2 was investigated in the absence of cyclohexene. Horseradish peroxidase assay was employed to obtain the concentration of H_2O_2 for solutions collected at different time point. Briefly, 600 μL of solution was sampled at a given time point followed by catalyst removal via centrifugation (12,000 rpm/5 min). 500 μL of supernatant was then collected and diluted 3 times by DI water (the total volume was 1.5 mL). This solution was subsequent mixed with another solution containing 20 μL of horseradish peroxidase (HRP, 1 unit), 200 μL tetramethylbenzidine (TMB, 5 mM) and 1.3 mL acetate buffer. The concentration of H_2O_2 can be determined by UV-Vis spectroscopy (Agilent Cary 60) based on the intensity of absorption peak at 652 nm (i.e., the oxidation of TMB).

2.8. Raman study

The configuration of adsorbed H_2O_2 on HNb_3O_8 samples was characterized at room temperature by a Bayspec Agility spectrometer ($\lambda = 785$ nm) with a resolution of 4 cm^{-1} . Typically, 10 mg catalyst was press into a thin wafer and then placed onto a custom-made sample holder. Once 5 μL H_2O_2 solution was dropped in one shot on the thin wafer, the laser of the Raman spectrometer was immediately turned on to record the corresponding signal.

2.9. Catalytic testing and product analysis

The catalytic epoxidation of cyclohexene with H_2O_2 over HNb_3O_8 samples was conducted in a batch reactor. The reactor consists of a two-neck round-bottomed flask, a temperature-controlled heater, a magnetic agitation and a condenser. In a typical experiment, 2 mmol cyclohexene and 100 mg catalyst were pre-mixed with 10 mL methanol. The reaction can be initiated by the addition of 0.175 mL H_2O_2 aqueous solution (30%) in one shot at a temperature ranging from 313 to 353 K. The product distribution was determined by gas chromatography-mass spectroscopy (GC-MS, Agilent 7890 A with 5975 C) equipped with a DB-5MS column. The initial and finish temperature of the oven, both of

which were held for 2 min, were 333 K and 523 K, respectively, at the heating rate of 10 K/min. The temperature of the injector was 523 K with a split of 150:1. The auxiliary temperature was 553 K and the rate of the helium flow was 1.0 mL/min. The products were further quantitatively analyzed by GC (Agilent 7890 A) equipped with an HP-5 column under the same condition as the GC-MS.

3. Results and discussion

3.1. Characterization of HNb_3O_8 samples

Few-layer HNb_3O_8 (f- HNb_3O_8) and single-layer HNb_3O_8 (s- HNb_3O_8) were hydrothermally synthesized according to our previous work [29]. Transmission electron microscopy (TEM) reveals a sheet-like morphology for both samples with lateral length up to several micrometers (Fig. 1a for f- HNb_3O_8 and Fig. 1b for s- HNb_3O_8). Atomic force microscopy (AFM) was further adopted for the evaluation of their thickness. As shown in Fig. 1c and Fig. 1d, the thickness of f- HNb_3O_8 and s- HNb_3O_8 is about 3.6 nm and 0.9 nm, confirming their few-layer and single-layer structure. Bulk HNb_3O_8 (b- HNb_3O_8) was also prepared for further comparison (Fig. S1). The XRD patterns of b- HNb_3O_8 (Fig. 1e) match very well with the PDF card of layered HNb_3O_8 (ICDD No.37-0833). Although no characteristic XRD peaks can be identified in both f- HNb_3O_8 and s- HNb_3O_8 , their Raman pattern (Fig. 1f) with a characteristic vibration of the edge-shared NbO_6 units at around 1000 cm^{-1} confirms that they share the unit structure of crystalline HNb_3O_8 [29]. Table 1 shows the corresponding surface area for each HNb_3O_8 sample. The lower surface area obtained for s- HNb_3O_8 (cf. f- HNb_3O_8) is probably due to the re-stacking of its single-layer structure (see Fig. S2 for details).

We believe a thorough surface understanding of solid catalysts is critical for the study of H_2O_2 activation and the product distribution for a given substrate. Since BA and Nb-based LA sites can interact differently with H_2O_2 , the surface acidic property of HNb_3O_8 samples was first evaluated by pyridine-assisted infrared (pyridine-IR). In general, pyridine adsorbed on BA and LA sites gives IR signals respectively at ca. 1640/1540 cm^{-1} and 1610/1450 cm^{-1} , while both types of acid sites also contribute to an extra band at 1490 cm^{-1} . As shown in Fig. 2a, only BA signals (1638/1540 cm^{-1}) can be identified on b- HNb_3O_8 , which is due to the bridged protons on its terminal surfaces (Scheme 1d). Interestingly, the reduction of layers of this material generates additional LA signals (1611/1450 cm^{-1}) on f- HNb_3O_8 and s- HNb_3O_8 . Since no shift in both BA and LA positions can be observed for HNb_3O_8 samples, this suggests that either (1) they have the same acidic “strength” or (2) the pyridine molecule is too basic to differentiate each of them [27]. To confirm this, a more advanced technique, probe-assisted NMR, was further employed. We showed recently that this technique is very powerful in reporting surface properties of metal oxides based on the ^{31}P chemical shifts ($\delta^{31}\text{P}$) of trimethylphosphine (TMP) [30–36]. Typically, the interaction between the lone pair of TMP and surface BA/LA sites can give ^{31}P resonances in distinct regions 0 to –6 ppm/–20 to –60 ppm. Because a BA/LA site with higher strength will form a stronger bond with TMP pushing $\delta^{31}\text{P}$ to downfield (i.e., positive ppm), the chemical shift of ^{31}P ($\delta^{31}\text{P}$) within each region can thus differentiate BA/LA strength among catalysts. Most importantly, the concentration of BA/LA sites at a specific strength can be obtained by the peak area at a $\delta^{31}\text{P}$ [27]. As shown in Fig. 2b, the strength of BA/LA sites of HNb_3O_8 samples can be well-resolved by TMP- ^{31}P NMR within each region. The BA signal $\delta^{31}\text{P}$ at –2.1 ppm (green highlighted) observed for all HNb_3O_8 samples suggests that the strength of bridged protons on terminal surfaces is independent of the number of layers. In contrast, the appearance and strength of LA sites seem to associate with sample thickness as evidenced by the weak ($\delta^{31}\text{P}$ at –40.4 ppm) and strong ($\delta^{31}\text{P}$ at –25.1 ppm) LA sites on f- HNb_3O_8 and s- HNb_3O_8 (Fig. 2b). Given limited information being revealed by conventional pyridine-IR, this highlights the importance of surface understanding of solid catalysts for

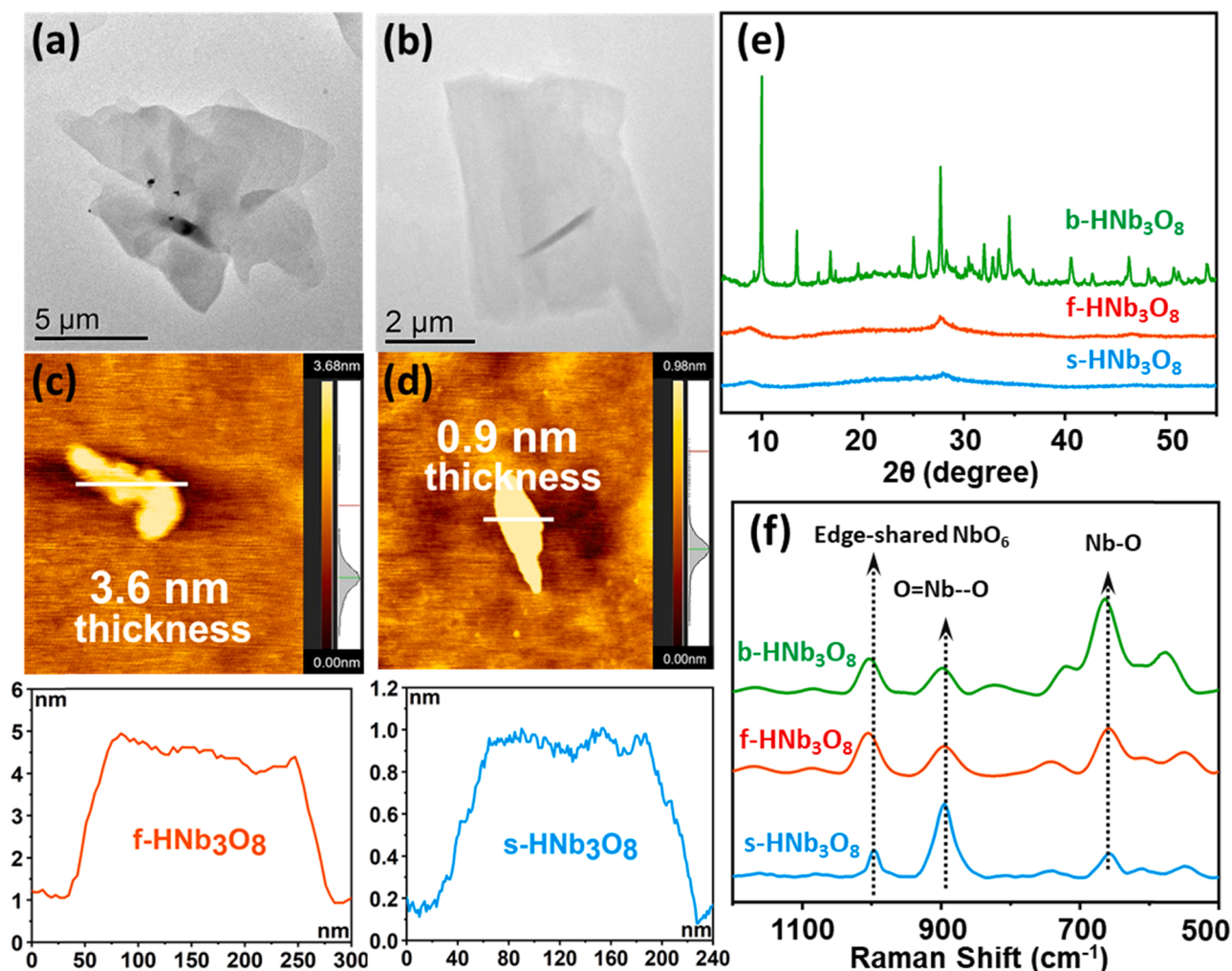


Fig. 1. TEM images of (a) f-HNb₃O₈, (b) s-HNb₃O₈, and (c, d) their corresponding thickness analysis by AFM. (e) XRD and (f) Raman spectra of HNb₃O₈ samples.

Table 1

Sample details such as surface area, acid site strength/concentration (from TMP-³¹P NMR), Nb⁴⁺/Nb⁵⁺ ratio (from XPS), and the coordination number of Nb (CN_{Nb}, from XAS).

Catalyst	Surface Area [m ² /g]	BA [μmol/g]			LA/BA Ratio	Nb ⁴⁺ /Nb ⁵⁺ Ratio	CN _{Nb}
		-2.1 ppm	-25.1 ppm (strong)	-40.4 ppm (weak)			
b-HNb ₃ O ₈	10	30	—	—	—	0.06	5.9
f-HNb ₃ O ₈	166	234	—	295	1.26	0.11	5.6
s-HNb ₃ O ₈	121	150	129	—	0.86	0.21	4.5

a precise structure-activity correlation [30–36]. Table 1 summarizes their qualitative and quantitative results of BA/LA sites provided by TMP-³¹P NMR. Note that the amount of either individual acid sites or their sum for HNb₃O₈ samples is in line with the trend of the corresponding surface area (i.e., f-HNb₃O₈ > s-HNb₃O₈ > b-HNb₃O₈).

To investigate the origin of these new LA sites on f-/s-HNb₃O₈, X-ray photoelectron spectroscopy (XPS) and X-ray absorption spectroscopy (XAS) results of HNb₃O₈ samples were further analyzed. A gradual shift of XPS Nb 3d_{3/2} and 3d_{5/2} peaks to lower binding energy can be observed from b-HNb₃O₈ to f-/s-HNb₃O₈ (Fig. 2c) with an increasing Nb⁴⁺/Nb⁵⁺ ratio (Fig. S3 and Table 1). This can be attributed to the formation of oxygen vacancies in f-/s-HNb₃O₈ due to the structural distortion of surface NbO₆ units. This result also agrees well with their Raman spectra (Fig. 1 f), which shows an increased signal of the distorted O=Nb–O at 890 cm⁻¹ at the expense of symmetric Nb–O at

660 cm⁻¹ (cf. b-HNb₃O₈) [37,38]. Since Nb⁴⁺ contributes a smaller pre-edge XAS peak than Nb⁵⁺ [39], the change of Nb⁴⁺/Nb⁵⁺ ratio between HNb₃O₈ samples should also reflect in their Nb K-edge XAS spectra (Fig. 2d). As expected, f-/s-HNb₃O₈ bears lower intensity for this peak compared to that of b-HNb₃O₈. The local structure of Nb atoms in those samples was further analyzed by the Fourier transformed Nb K-edge extended X-ray absorption fine structure (EXAFS) technique (Fig. S4 and Table S1). The coordination number of Nb (CN_{Nb}) for b-HNb₃O₈ (i.e., 5.9) matches well with the theoretical number of 6 for NbO₆ layered structures, while this number decreases to 5.6 for f-HNb₃O₈ and 4.5 for s-HNb₃O₈ with an increasing Nb⁴⁺/Nb⁵⁺ ratio (Table 1). Therefore, the emerging of those LA sites for f-/s-HNb₃O₈ can be attributed to the formation of lower coordinate NbO₅/NbO₄ (or oxygen vacancies) in surface distorted NbO₆ units [40]. The degree of this distortion was found to positively associate with their LA strength. For

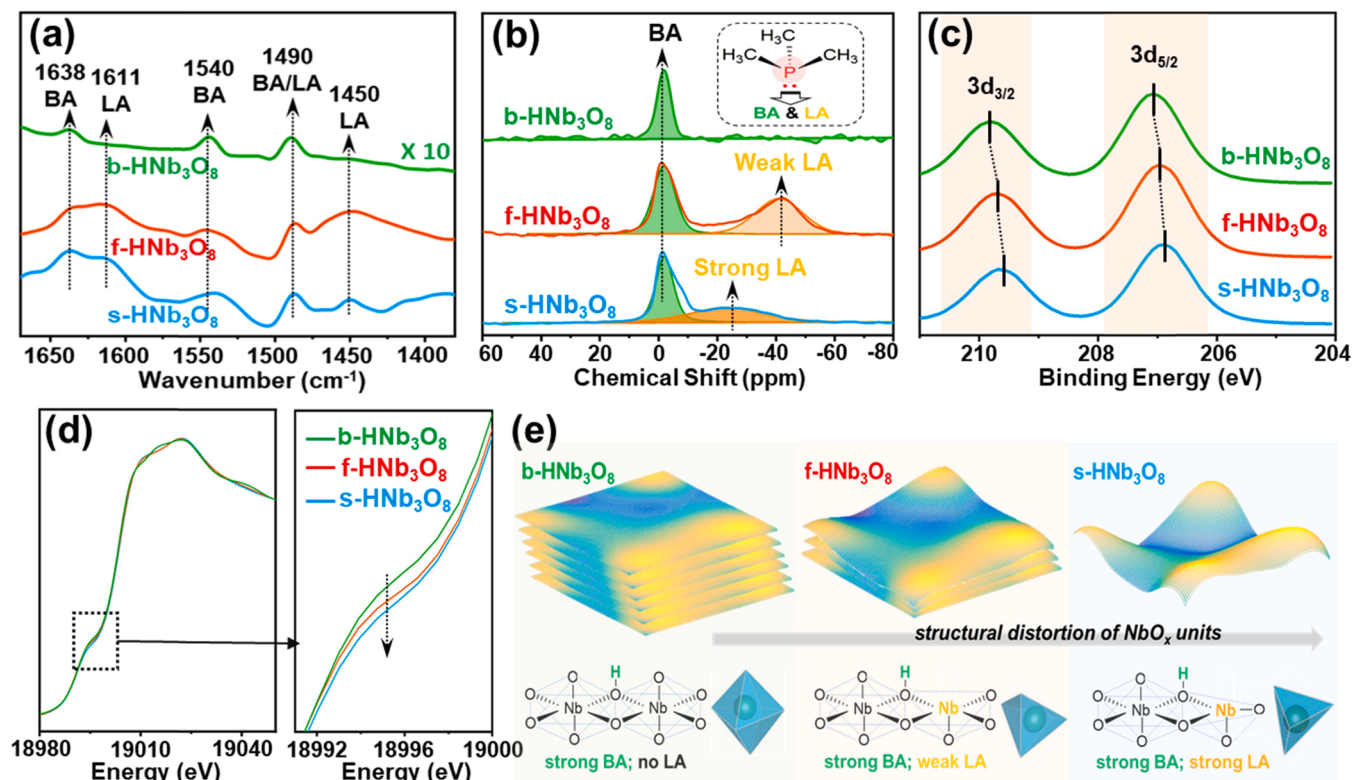


Fig. 2. (a) Pyridine-IR, (b) TMP-³¹P NMR, (c) XPS and (d) XAS Nb K-edge spectra of HNb₃O₈ samples. (e) Schematic illustration of the emerging of Nb sites and their Lewis acidity in distorted NbO_x units during the bulk-to-nano engineering of HNb₃O₈.

example, f-HNb₃O₈ with less distorted Nb centers ($CN_{Nb} = 5.6$) shows weak LA strength ($\delta^{31}P$ at -40.4 ppm) while s-HNb₃O₈ with highly distorted Nb centers ($CN_{Nb} \sim 4.5$) exhibits strong LA strength ($\delta^{31}P$ at -25.1 ppm) (Fig. 2b). Interestingly, the distortion of surface NbO_x units for both samples seems to have a negligible effect on the strength of their BA sites ($\delta^{31}P$ at -2.1 ppm, cf. b-HNb₃O₈). Fig. 2e schematically illustrates the origin of these exposed Nb sites and their Lewis acidity for f-/s-HNb₃O₈ samples.

3.2. Selective activation of H₂O₂

HNb₃O₈ samples with distinct surface features are believed to adsorb/activate H₂O₂ differently. As shown in Fig. 3a, a sudden drop in H₂O₂ concentration ($[H_2O_2]$) to around 70% can be observed for all samples in the first 5 min of reaction. Interestingly, $[H_2O_2]$ maintains at this level for s-HNb₃O₈ while it gradually decreases with time for b-/f-HNb₃O₈. Since H₂O₂ disproportionation often associates with the generation of radicals, terephthalic acid (TA) was then used as a probe since it forms fluorescent 2-hydroxy-terephthalic acid (TAOH, at 430 nm) specifically with free OH radicals (Fig. 3b). A surge of OH radicals was observed for all HNb₃O₈ samples in the first 5 mins presumably due to the reach of a new equilibrium between catalysts' surface and H₂O₂ in a fresh solution. This explains the considerable drop of their $[H_2O_2]$ at the very beginning of the reaction (Fig. 3a). Later on, the intensity of the fluorescent signal increases gradually with time on b-/f-HNb₃O₈ while surprisingly no such change in intensity can be seen for s-HNb₃O₈ (Fig. 3b). This result not only agrees well with the change of their $[H_2O_2]$ but also strongly suggests that H₂O₂ was activated very differently on s-HNb₃O₈. The silence of H₂O₂ disproportionation on s-HNb₃O₈ can be further confirmed by electron paramagnetic resonance (EPR) using 5,5-dimethyl-1-pyrroline N-oxide (DMPO) as a radical trap. As expected, the increase of DMPO-OH with 1:2:2:1 resonance intensity (Fig. 3c) and DMPO-OOH with six resonance lines (Fig. 3d) were both identified on b-/f-HNb₃O₈ as reaction proceeds while not for s-HNb₃O₈. Note that the

analysis of HO₂ radicals was conducted in methanol (i.e., to remove OH radicals) because DMPO-OOH has relatively slow kinetics of formation (cf. DMPO-OH) [41].

To gain an insight into the role of BA/LA sites, we first compared b-HNb₃O₈ with f-HNb₃O₈ because they possess the same BA sites ($\delta^{31}P$ at -2.1 ppm) but extra weak LA sites ($\delta^{31}P$ at -40.4 ppm) for f-HNb₃O₈. The amount of H₂O₂ consumed or radicals produced over b-/f-HNb₃O₈ (Fig. 3) was found not proportional to their surface area or concentration of BA sites (Table 1). To be more specific, f-HNb₃O₈ with a much higher surface area (16 times) and BA concentration (8 times) only consumes/produces about twice the amount of H₂O₂/radicals (cf. b-HNb₃O₈), indicating that the presence of LA sites hinders the adsorbed H₂O₂ from its decomposition promoted by BA sites. One may thus expect that the sample with higher LA concentration and LA/BA ratio should better suppress H₂O₂ disproportionation. However, s-HNb₃O₈ with lower LA concentration and LA/BA ratio (cf. f-HNb₃O₈, Table 1) further quenches the decomposition of H₂O₂. Given both samples bearing the same BA sites ($\delta^{31}P$ at -2.1 ppm), the muted H₂O₂ disproportionation observed on s-HNb₃O₈ could be exclusively attributed to its strong LA sites ($\delta^{31}P$ at -25.1 ppm). Above results clearly show that even a single material (i.e., HNb₃O₈) can interact very differently with H₂O₂ affecting its activation pathway and hence utilization. The complex catalysts often used in the literature and characterized by surface techniques with low resolution could both make the mechanistic study very difficult [27,28].

In fact, the surface information of HNb₃O₈ samples gained from TMP-³¹P NMR (Fig. 2b) further allows an in-depth discussion (cf. pyridine-IR). For example, the decomposition of H₂O₂ is greatly promoted by BA sites alone on b-HNb₃O₈, while f-HNb₃O₈ and s-HNb₃O₈ bearing extra LA sites with distinct local structures/chemical states hinders this activation pathways to a certain degree. Raman was further adopted for an insight into the adsorption configuration of H₂O₂ and its later activation on the latter two samples [16]. For s-HNb₃O₈ (Fig. 4a), a gradual increase in Raman signal at 610 cm⁻¹ suggests the bidentate chelation of H₂O₂ to Nb centers [42], which facilitates the formation of

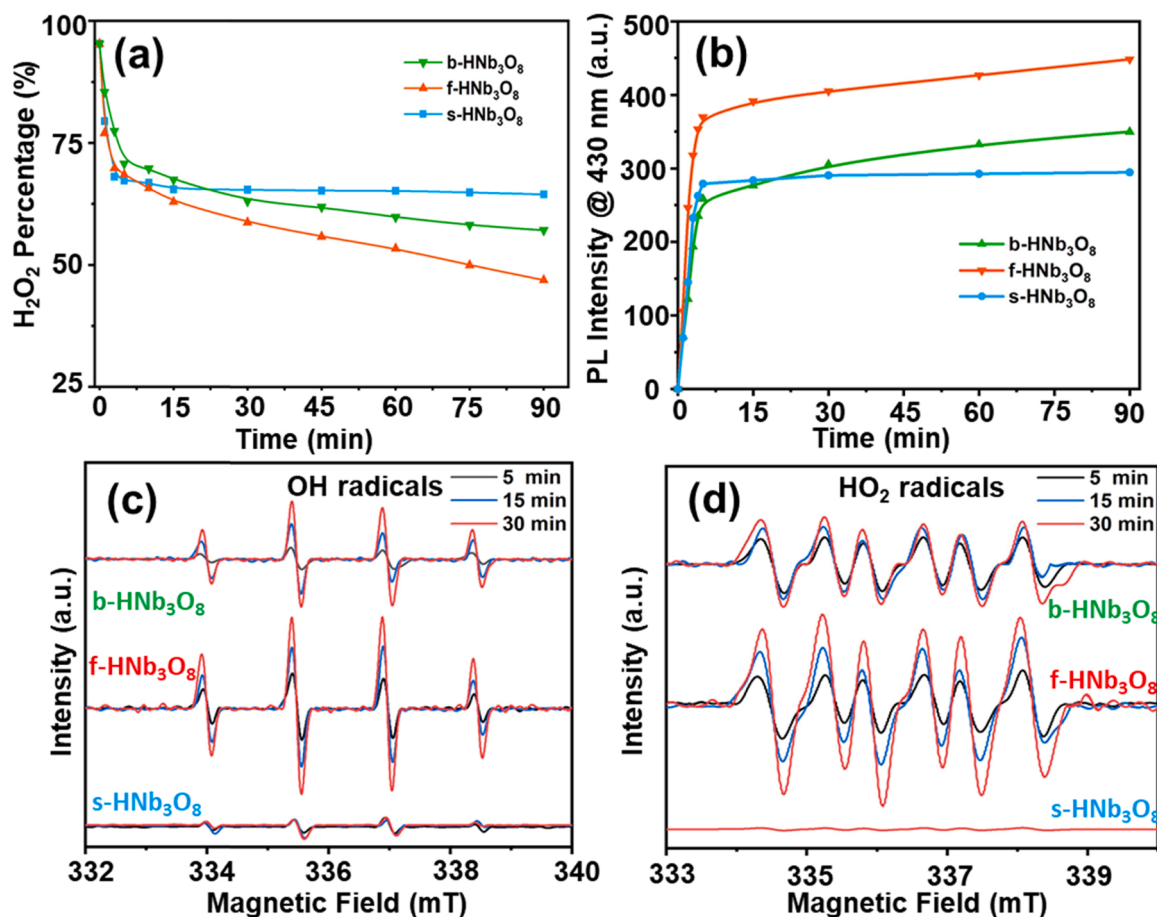


Fig. 3. (a) The disproportionation of H_2O_2 and (b) the generation of OH radicals (using terephthalic acid as probe) over HNb_3O_8 samples. EPR evaluating the production of (c) OH radicals in water and (d) HO_2 radicals in methanol with time using DMPO as radical trap for HNb_3O_8 samples.

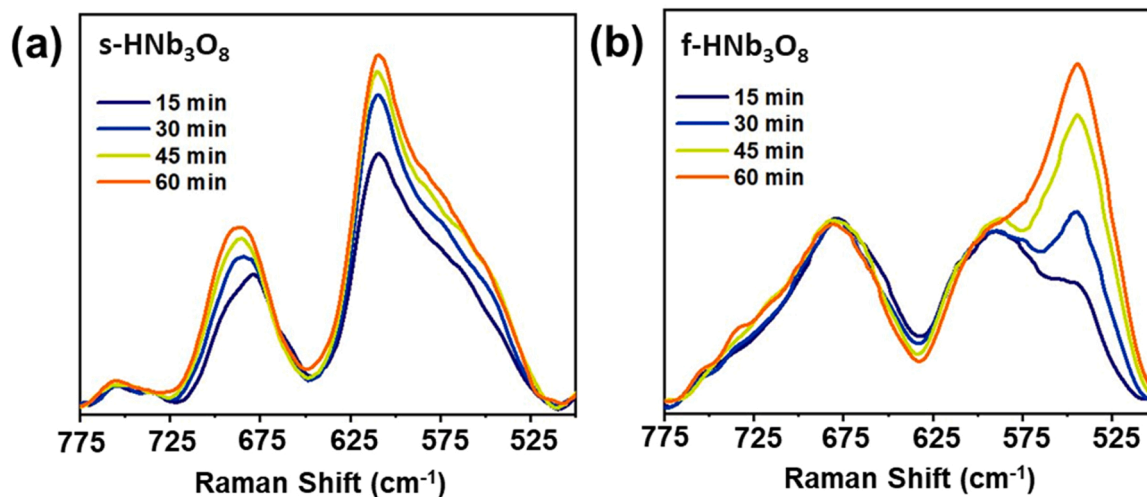


Fig. 4. Raman spectra of H_2O_2 adsorbed (a) s- HNb_3O_8 and (b) f- HNb_3O_8 as a function of time.

$\text{Nb}-\eta_2-\text{O}_2$ species. The $\text{Nb}-\text{O}$ signal at 680 cm^{-1} also increases with time presumably due to the protonation of some $\text{Nb}-\eta_2-\text{O}_2$ (i.e., the formation of $\text{Nb}-\eta_2-\text{OOH}$) by nearby BA sites, leaving polarized O-O bond. Those bidentate Nb-peroxo species are very stable on s- HNb_3O_8 with no radicals produced in the presence of free H_2O_2 (Fig. 3). The BA-promoted disproportionation of H_2O_2 could thus be quenched on this sample. Interestingly, no change of Raman signal at both positions can be

observed for f- HNb_3O_8 (Fig. 4b) but a peak of monodentate Nb-peroxo species (likely $\text{Nb}-\text{OOH}$) at 545 cm^{-1} evolving with time [42]. Given that the CN_{Nb} is 4.5 for s- HNb_3O_8 and 5.6 for f- HNb_3O_8 (Table 1), this explains why the bidentate adsorption of H_2O_2 is preferred on the former and monodentate on the latter. This monodentate Nb-peroxo species on f- HNb_3O_8 may stabilize nearby BA sites by its non-Nb-attached oxygen via hydrogen bond interaction, resulting in the hindered H_2O_2

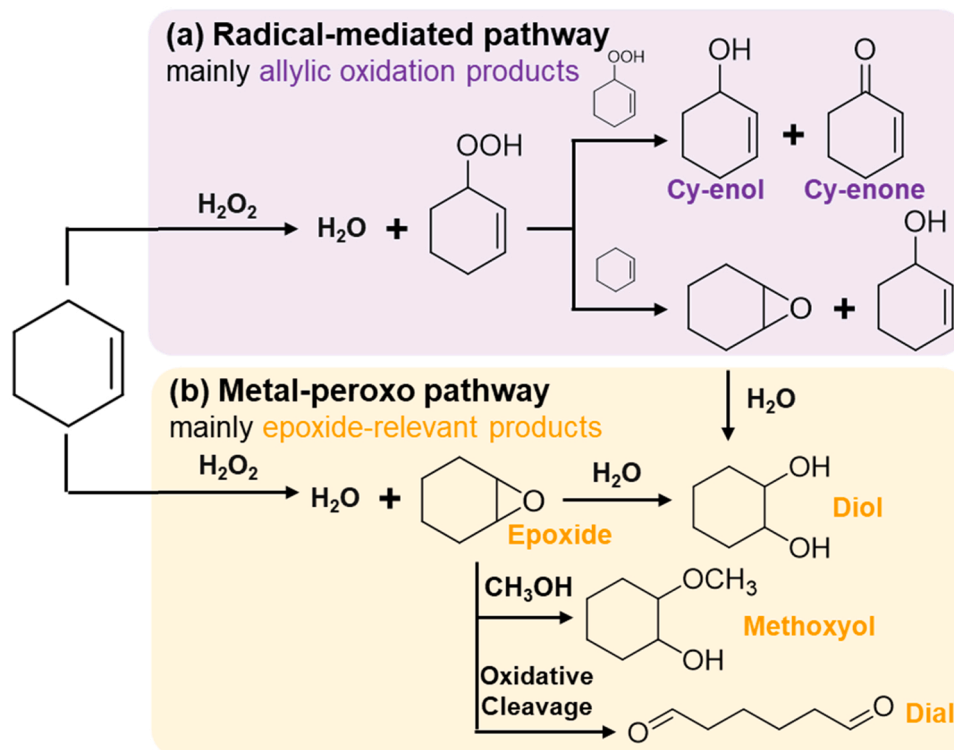
disproportionation (cf. b-HNb₃O₈). To conclude, LA sites can suppress H₂O₂ disproportionation induced by BA sites and the degree of this alleviation is closely associated with their local structures/chemical states.

3.3. Cyclohexene oxidation with H₂O₂

The understanding of the interplay between H₂O₂ and HNb₃O₈ samples above is believed to explain the product distribution for a given substrate. Herein, we chose cyclohexene as the substrate since the distribution of its oxidized forms is closely associated with how H₂O₂ is activated (Scheme 2) [18–26]. Table 2 shows the yield of allylic oxidation/epoxide-relevant products for HNb₃O₈ samples in methanol at 333 K for 1 hr. The radical-mediated pathway (Scheme 2a) produces cyclohexenol (Cy-enol) and cyclohexanone (Cy-enone) via a reaction of two cyclohexenyl hydroperoxide intermediates. One cyclohexenyl hydroperoxide intermediate can also react with a cyclohexene to produce epoxide and cyclohexanol. This very well explains the product distribution for b-HNb₃O₈ (entry 2), which solely undergoes the radical-mediated pathway. Although this pathway generates some epoxide, the time-dependent yield of allylic oxidation products for HNb₃O₈ samples (Fig. 5a) agrees well with their HO₂ radicals generated in Fig. 3d (i.e., f-HNb₃O₈ > b-HNb₃O₈ > s-HNb₃O₈). Note that OH radicals should be mostly removed by methanol solvent. The presence of surface LA sites indeed plays a key role hindering H₂O₂ disproportionation here. Bear in mind that f-HNb₃O₈ with a much higher surface area/BA concentration only produces about twice the concentration of radicals (cf. b-HNb₃O₈). This accounts for the doubled amount of allylic oxidation products observed for f-HNb₃O₈ (entry 3). For s-HNb₃O₈ with stronger LA (or more distorted Nb) sites, the yield of allylic oxidation products is even lower than b-HNb₃O₈ at all time points (Fig. 5a) due to the saturation of their concentration at the beginning of the reaction (see Fig. S5 for the yield of Cy-enol/Cy-enone with time). As one can expect, this is owing to the surge of radicals in the first 5 mins followed by the quenched H₂O₂ disproportionation on this sample for the rest of the

reaction time (Fig. 3).

The oxidation of cyclohexene by surface metal-peroxo species also produces epoxide but at a much higher rate (Table 2). Since no dissolved Nb species was detected by inductively coupled plasma atomic emission spectroscopy (ICP-AES), the Sheldon-type hot filtrate experiment thus confirms that the observed epoxides is due to the added catalysts (Fig. S6) [43]. However, the presence of LA sites further converts epoxide into three epoxide-derived products, namely 2-methoxycyclohexan-1-ol (methoxyol), cyclohexane-1,2-diol (diol), and adipaldehyde (dial) (Scheme 2b). This was further confirmed using cyclohexene oxide as the starting compound (see Table S2 and Scheme S1 for details). Fig. 5b shows the total yield of epoxide-relevant products for HNb₃O₈ samples as a function of reaction time. Apparently, this pathway was facilitated in an order (s-HNb₃O₈ > f-HNb₃O₈ > b-HNb₃O₈) different from that of the radical-mediated one (Fig. 5a). Given this pathway being completely suppressed on b-HNb₃O₈, the presence of LA sites on f-/s-HNb₃O₈ thus promotes the generation of epoxide and its further conversion. However, their “quantity” seems not the dominant factor as s-HNb₃O₈ with fewer LA sites (Table 1) provides a much higher yield of epoxide-relevant products than f-HNb₃O₈ (Fig. 5b). Instead, the “quality” of LA sites (i.e., strength and local structure) is believed to play a key role affecting the reactivity of Nb-peroxo species. To confirm this, the turnover frequency (TOF) was further calculated for f-/s-HNb₃O₈ according to the number of their surface LA sites obtained by TMP-³¹P NMR. The TOF is defined herein as the moles of the epoxide-relevant products generated per mole of surface LA sites per hour. As shown in Fig. 5c, the initial TOF in the first 15 min for s-HNb₃O₈ (145.7 h^{−1}) is about 7.7 times higher than f-HNb₃O₈ (18.9 h^{−1}), suggesting that the bidentate Nb-peroxo species (i.e., Nb-η₂-O₂/Nb-η₂-OOH) is much active than its monodentate counterpart (i.e., Nb-OOH) in cyclohexene epoxidation. Given the quenched H₂O₂ disproportionation on s-HNb₃O₈, the concentration of H₂O₂ was found to decrease with cyclohexene after ca. 5 mins of the reaction (Fig. 5d) achieving the stoichiometric utilization of H₂O₂. Although LA sites further catalyze the conversion of epoxide, the optimization of product distribution for this pathway (e.g., tuning



Scheme 2. Cyclohexene oxidation with H₂O₂ via (a) radical-mediated pathway with mainly allylic oxidation products and (b) metal-peroxo species with mainly epoxide-relevant products.

Table 2

Cyclohexene oxidation with H₂O₂ over HNb₃O₈ samples and the yield of epoxide-relevant/allylic oxidation products. Reaction conditions: 2 mM cyclohexene, 2 mM H₂O₂, 10 mL CH₃OH, 333 K.

Entry	Catalyst	Cyclohexene Conversion [%]	Epoxide-relevant products Yield [%]				Allylic oxidation products Yield [%]	
			Epoxide	Methoxyol	Diol	Dial	Cy-enol	Cy-enone
1	–	0.2	0.1	–	–	–	0.1	–
2	b-HNb ₃ O ₈	13	5	–	–	–	4	3
3	f-HNb ₃ O ₈	39	11	5.5	6	2	8	5
4	s-HNb ₃ O ₈	78	41	25	1	5	1.5	1
5	s-HNb ₃ O ₈ -e	34	13	7	3	2	6	3

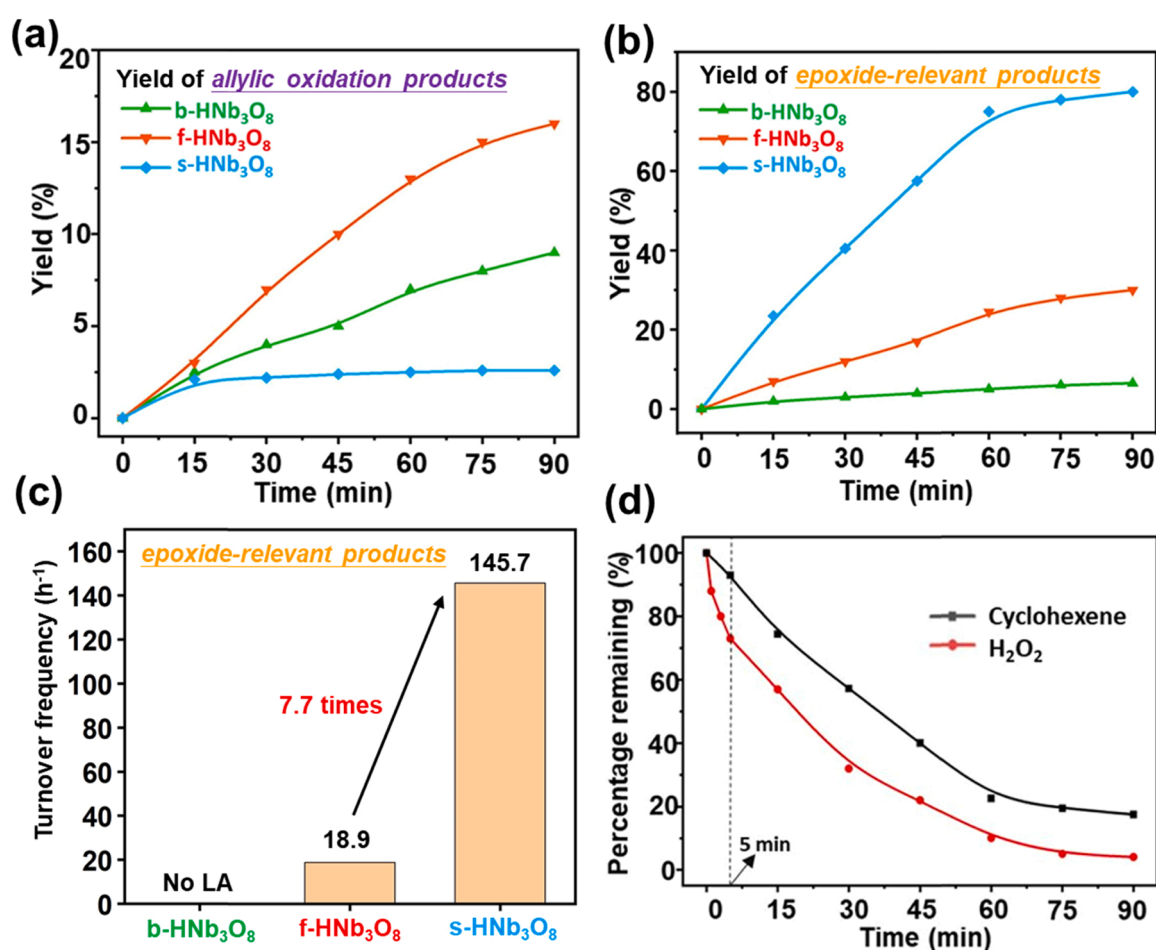


Fig. 5. The yield of (a) allylic oxidation products and (b) epoxide-relevant products over HNb₃O₈ samples as a function of time. (c) The initial TOF (h⁻¹) in the first 15 min calculated for epoxide-relevant molecules based on the number of exposed Nb (or LA) sites. (d) The conversion of cyclohexene and H₂O₂ over s-HNb₃O₈ with time.

temperature and solvent, Table S3) is out of the scope of this study.

Finally, it could be very interesting to know the difference in the reactivity between bidentate Nb-peroxo species (i.e., Nb-η₂-O₂ vs. Nb-η₂-OOH with polarized O-O bond) in this reaction. We then adopted a typical Na⁺ exchange method to replace the bridged protons on s-HNb₃O₈. Although this treatment is believed to remove some BA sites [44], TMP-³¹P NMR result of the exchanged sample (denoted as s-HNb₃O₈-e) shows an increased concentration for both BA and LA sites

instead (Fig. S7a) presumably due to the reduced sample re-stacking. A considerable shift of δ³¹P to ca. −40 ppm can also be observed for LA sites but not for BA sites after the treatment. The weakened LA strength is indeed associated with the structural change of Nb sites on s-HNb₃O₈-e as evidenced by the decreased Raman signal at 890 cm⁻¹ (i.e., the distorted O=Nb-O, Fig. S7b). Accordingly, the ion exchange method may not remove BA as effective as stated in the literature and can further affect the strength of LA in our case, making it very difficult

to distinguish the reactivity of bidentate Nb-peroxo species here. Despite this, s-HNb₃O₈-e with comparable local Nb structure and LA strength as that of f-HNb₃O₈ (Fig. S7a) was found to provide a similar product distribution in cyclohexene oxidation with H₂O₂ (Table 2). Fig. S8 shows the corresponding yield of allylic oxidation and epoxide-relevant products with time. As one can expect, H₂O₂ disproportionation was not quenched on this post-treated sample, which results in an increasing amount of allylic oxidation products with time (Fig. S8a). This result confirms again that the “quality” of LA sites on HNb₃O₈ is the key factor dictating the configuration/reactivity of Nb-peroxo species in H₂O₂ activation and hence the product distribution for a given substrate.

4. Conclusions

In summary, an in-depth surface understanding of HNb₃O₈ samples from bulk to nano was conducted with supports from a wide range of techniques. As revealed by NMR and XAS, the reduction of layers of this material generates LA sites due to the distortion of surface NbO₆ units. The degree of this distortion was found to positively associate with their LA strength while not for BA sites originally preserved on the terminal surfaces. This allows us to study the individual/synergistic role of BA and LA sites in H₂O₂ activation and later substrate oxidation. As expected, BA sites on b-HNb₃O₈ promote H₂O₂ disproportionation via radical-mediated pathway, giving low H₂O₂ utilization and allylic oxidation products in alkene oxidation. This pathway, however, can be suppressed to a certain degree in the presence of LA sites depending on their local structures and chemical states. For example, the adsorption of H₂O₂ on f-HNb₃O₈ gives monodentate Nb-species, which not only promotes alkene epoxidation but hinders H₂O₂ disproportionation. The latter reaction was even found quenched by the bidentate Nb-species formed on s-HNb₃O₈. This, together with their high TOF for cyclohexene epoxidation, makes s-HNb₃O₈ a promising catalyst with a near stoichiometric H₂O₂-to-epoxide conversion. This work thus highlights a facile regulation of H₂O₂ activation pathway by bulk-to-nano engineering of layered materials and provides insights into their design for high H₂O₂ utilization in selective oxidation reaction.

CRediT authorship contribution statement

Guohan Sun: Methodology, Investigation, Writing – original draft. **Molly Meng-Jung Li:** Formal analysis, Software. **Keizo Nakagawa:** Resources. **Guangchao Li:** Validation. **Tai-Sing Wu:** Data curation. **Yung-Kang Peng:** Conceptualization, Writing – original draft, Writing – review & editing, Supervision, Funding acquisition.

Declaration of Competing Interest

The authors declare the following financial interests/personal relationships which may be considered as potential competing interests: Yung Kang Peng reports financial support was provided by National Natural Science Foundation of China. Yung Kang Peng reports financial support was provided by Guangdong Basic and Applied Basic Research Foundation. Yung Kang Peng reports financial support was provided by Hong Kong Research Grants Council. Yung Kang Peng reports financial support was provided by Chow Sang Sang Group Research Fund.

Acknowledgements

We thank the National Natural Science Foundation of China (21902138), Guangdong Basic and Applied Basic Research Foundation (2021A1515010064), the Hong Kong Research Grants Council (CityU 21301719, CityU 11300020 and CityU 11305721), and Chow Sang Sang Group Research Fund (9229063) sponsored by Chow Sang Sang Holdings International Limited for funding support. We acknowledge the University Research Facilities in Materials Research Centre (MRC) and Chemical and Environmental Analysis (UCEA) of PolyU for experiments

support.

Appendix A. Supporting information

Supplementary data associated with this article can be found in the online version at doi:10.1016/j.apcatb.2022.121461.

References

- [1] I.A. Salen, M. El-Maazawi, A.B. Zaki, Kinetics and mechanisms of decomposition reaction of hydrogen peroxide in presence of metal complexes, *Int. J. Chem. Kinet.* 32 (2000) 634–666.
- [2] F. Cavani, J.H. Teles, Sustainability in catalytic oxidation: an alternative approach or a structural evolution? *ChemSusChem* 2 (2009) 508–534.
- [3] G. Goor, Hydrogen peroxide: manufacture and industrial use for production of organic chemicals, in: G. Strukul (Ed.), *Catalytic Oxidations with Hydrogen Peroxide as Oxidant*, Springer, 2013, pp. 13–44.
- [4] R. Goyal, O. Singh, A. Agrawal, C. Samanta, B. Sarkar, Advantages and limitations of catalytic oxidation with hydrogen peroxide: from bulk chemicals to lab scale process, *Catal. Rev.* (2020) 1–57.
- [5] R.J. Lewis, G.J. Hutchings, Recent advances in the direct synthesis of H₂O₂, *ChemCatChem* 11 (2018) 298–308.
- [6] F. Li, Q. Shao, M. Hu, Y. Chen, X. Huang, Hollow Pd–Sn nanocrystals for efficient direct H₂O₂ synthesis: the critical role of Sn on structure evolution and catalytic performance, *ACS Catal.* 8 (2018) 3418–3423.
- [7] G.H. Han, S.H. Lee, S.Y. Hwang, K.Y. Lee, Advanced development strategy of nano catalyst and DFT calculations for direct synthesis of hydrogen peroxide, *Adv. Energy Mater.* 11 (2021) 2003121.
- [8] Y. Zhong, X. Liang, Z. He, W. Tan, J. Zhu, P. Yuan, R. Zhu, H. He, The constraints of transition metal substitutions (Ti, Cr, Mn, Co and Ni) in magnetite on its catalytic activity in heterogeneous Fenton and UV/Fenton reaction: from the perspective of hydroxyl radical generation, *Appl. Catal. B Environ.* 150–151 (2014) 612–618.
- [9] C. Zang, X. Zhang, S. Hu, F. Chen, The role of exposed facets in the Fenton-like reactivity of CeO₂ nanocrystal to the Orange II, *Appl. Catal. B Environ.* 216 (2017) 106–113.
- [10] J. Yang, D. Zeng, Q. Zhang, R. Cui, M. Hassan, L. Dong, J. Li, Y. He, Single Mn atom anchored on N-doped porous carbon as highly efficient Fenton-like catalyst for the degradation of organic contaminants, *Appl. Catal. B Environ.* 279 (2020), 119363.
- [11] T. Yang, D. Yu, D. Wang, T. Yang, Z. Li, M. Wu, M. Petru, J. Crittenden, Accelerating Fe(III)/Fe(II) cycle via Fe(II) substitution for enhancing Fenton-like performance of Fe-MOFs, *Appl. Catal. B Environ.* 286 (2021), 119859.
- [12] Q. Xia, D. Zhang, Z. Yao, Z. Jiang, Investigation of Cu heteroatoms and Cu clusters in Fe–Cu alloy and their special effect mechanisms on the Fenton-like catalytic activity and reusability, *Appl. Catal. B Environ.* 299 (2021), 120662.
- [13] B. Yuan, H.-L. Chou, Y.-K. Peng, Disclosing the origin of transition metal oxides as peroxidase (and catalase) mimetics, *ACS Appl. Mater. Interfaces* (2021) doi.org/10.1021/acsami.1c13429.
- [14] J. Zhang, T.-S. Wu, H.V. Thang, K.-Y. Tseng, X. Hao, B. Xu, H.-Y. Chen, Y.-K. Peng, Cluster nanozymes with optimized reactivity and utilization of active sites for effective peroxidase (and oxidase) mimicking, *Small* 18 (2022) 2104844.
- [15] Y. Zhu, R. Zhu, Y. Xi, J. Zhu, G. Zhu, H. He, Strategies for enhancing the heterogeneous Fenton catalytic reactivity: a review, *Appl. Catal. B Environ.* 255 (2019), 117739.
- [16] Z. Tan, J. Zhang, Y.C. Chen, J.P. Chou, Y.K. Peng, Unravelling the role of structural geometry and chemical state of well-defined oxygen vacancies on pristine CeO₂ for H₂O₂ activation, *J. Phys. Chem. Lett.* 11 (2020) 5390–5396.
- [17] J. Zhang, Z. Tan, W. Leng, Y.C. Chen, S. Zhang, B.T.W. Lo, K.K.L. Yung, Y.K. Peng, Chemical state tuning of surface Ce species on pristine CeO₂ with 2400% boosting in peroxidase-like activity for glucose detection, *Chem. Commun.* 56 (2020) 7897–7900.
- [18] A.C. Silva, R.M. Cepera, M.C. Pereira, D.Q. Lima, J.D. Fabris, L.C.A. Oliveira, Heterogeneous catalyst based on peroxo-niobium complexes immobilized over iron oxide for organic oxidation in water, *Appl. Catal. B Environ.* 107 (2011) 237–244.
- [19] M. Ziolek, I. Sobczak, P. Decyk, K. Sobańska, P. Pietrzyk, Z. Sojka, Search for reactive intermediates in catalytic oxidation with hydrogen peroxide over amorphous Niobium(V) and Tantalum(V) oxides, *Appl. Catal. B Environ.* 164 (2015) 288–296.
- [20] N.E. Thornburg, S.L. Nauert, A.B. Thompson, J.M. Notestein, Synthesis–structure–function relationships of silica-supported Niobium(V) catalysts for alkene epoxidation with H₂O₂, *ACS Catal.* 6 (2016) 6124–6134.
- [21] D.T. Bregante, D.W. Flaherty, Periodic trends in olefin epoxidation over group IV and V framework-substituted zeolite catalysts: a kinetic and spectroscopic study, *J. Am. Chem. Soc.* 139 (2017) 6888–6898.
- [22] N.V. Maksimchuk, G.M. Maksimov, V.Y. Evtushok, I.D. Ivanchikova, Y.A. Chesalov, R.I. Maksimovskaya, O.A. Kholdeeva, A. Solé-Daura, J.M. Poblet, J.J. Carbó, Relevance of protons in heterolytic activation of H₂O₂ over Nb(V): insights from model studies on Nb-substituted polyoxometalates, *ACS Catal.* 8 (2018) 9722–9737.
- [23] D.T. Bregante, N.E. Thornburg, J.M. Notestein, D.W. Flaherty, Consequences of confinement for alkene epoxidation with hydrogen peroxide on highly dispersed group 4 and 5 metal oxide catalysts, *ACS Catal.* 8 (2018) 2995–3010.
- [24] D.T. Bregante, A.M. Johnson, A.Y. Patel, E.Z. Ayala, M.J. Cordon, B.C. Bukowski, J. Greeley, R. Gounder, D.W. Flaherty, Cooperative effects between hydrophilic

- pores and solvents: catalytic consequences of hydrogen bonding on alkene epoxidation in zeolites, *J. Am. Chem. Soc.* 141 (2019) 7302–7319.
- [25] N.V. Maksimchuk, V.Y. Evtushok, O.V. Zalomaeva, G.M. Maksimov, I. D. Ivanchikova, Y.A. Chesalov, I.V. Eltsov, P.A. Abramov, T.S. Glazneva, V. V. Yanshole, O.A. Kholdeeva, R.J. Errington, A. Solé-Daura, J.M. Poblet, J.J. Carbó, Activation of H₂O₂ over Zr(IV) insights from model studies on Zr-monosubstituted lindqvist tungstates, *ACS Catal.* 11 (2021) 10589–10603.
- [26] Y. Chen, S. Ahn, M.R. Mian, X. Wang, Q. Ma, F.A. Son, L. Yang, K. Ma, X. Zhang, J. M. Notestein, O.K. Farha, Modulating chemical environments of metal–organic framework-supported molybdenum(VI) catalysts for insights into the structure–activity relationship in cyclohexene epoxidation, *J. Am. Chem. Soc.* (2022) doi.org/10.1021/jacs.1c12421.
- [27] A. Zheng, S.B. Liu, F. Deng, ³¹P NMR chemical shifts of phosphorus probes as reliable and practical acidity scales for solid and liquid catalysts, *Chem. Rev.* 117 (2017) 12475–12531.
- [28] Y.-K. Peng, S.C.E. Tsang, Facet-dependent photocatalysis of nanosize semiconductive metal oxides and progress of their characterization, *Nano Today* 18 (2018) 15–34.
- [29] K. Nakagawa, T. Jia, W. Zheng, S.M. Fairclough, M. Katoh, S. Sugiyama, S. C. Tsang, Enhanced photocatalytic hydrogen evolution from water by niobate single molecular sheets and ensembles, *Chem. Commun.* 50 (2014) 13702–13705.
- [30] Y.-K. Peng, L. Ye, J. Qu, L. Zhang, Y. Fu, I.F. Teixeira, I.J. McPherson, H. He, S. C. Tsang, Trimethylphosphine-assisted surface fingerprinting of metal oxide nanoparticle by ³¹P solid-state NMR: a zinc oxide case study, *J. Am. Chem. Soc.* 138 (2016) 2225–2234.
- [31] Y.-K. Peng, Y. Hu, H.L. Chou, Y. Fu, I.F. Teixeira, L. Zhang, H. He, S.C.E. Tsang, Mapping surface-modified titania nanoparticles with implications for activity and facet control, *Nat. Commun.* 8 (2017) 675.
- [32] Y.-K. Peng, H.-L. Chou, S.C.E. Tsang, Differentiating surface titanium chemical states of anatase TiO₂ functionalized with various surface groups, *Chem. Sci.* 9 (2018) 2493–2500.
- [33] Y.-K. Peng, B. Keeling, Y. Li, J. Zheng, T. Chen, H.-L. Chou, T.J. Puchler, R. A. Taylor, S.C.E. Tsang, Unravelling the key role of surface features behind facet-dependent photocatalysis of anatase TiO₂, *Chem. Commun.* 55 (2019) 4415–4418.
- [34] Z. Tan, T.-S. Wu, Y.-L. Soo, Y.-K. Peng, Unravelling the true active site for CeO₂-catalyzed dephosphorylation, *Appl. Catal. B Environ.* 264 (2020), 118508.
- [35] Z. Tan, G. Li, H.-L. Chou, Y. Li, X. Yi, A.H. Mahadi, A. Zheng, S.C. Edman Tsang, Y.-K. Peng, Differentiating surface Ce species among CeO₂ facets by solid-state NMR for catalytic correlation, *ACS Catal.* 10 (2020) 4003–4011.
- [36] Q. Wang, X. Yi, Y.-C. Chen, Y. Xiao, A. Zheng, J.L. Chen, Y.-K. Peng, Electronic-state manipulation of surface titanium activates dephosphorylation over TiO₂ near room temperature, *Angew. Chem. Int. Ed.* 133 (2021) 16285–16291.
- [37] J.M. Jehng, I.E. Wachs, Structural chemistry and Raman spectra of niobium oxides, *Chem. Mater.* 3 (1991) 100–107.
- [38] I.E. Wachs, C.A. Roberts, Monitoring surface metal oxide catalytic active sites with Raman spectroscopy, *Chem. Soc. Rev.* 39 (2010) 5002–5017.
- [39] R. Morea, J. Gonzalo, J. Siegel, J. Solis, Structural Assessment of Unconventional Lead Niobium Germanate Glasses with Large Nb Contents by High Resolution Xanes & X-Ray Emission Spectroscopy, Experiment Report. Beamline ID26 at ESRF Grenoble 2013.
- [40] A. Takagaki, D. Lu, J.N. Kondo, M. Hara, S. Hayashi, K. Domen, Exfoliated HNb₃O₈ nanosheets as a strong protonic solid acid, *Chem. Mater.* 17 (2005) 2487–2489.
- [41] A.C. Moreno Maldonado, E.L. Winkler, M. Raineri, A. Toro Córdova, L. M. Rodríguez, H.E. Troiani, M.L. Mojica Pesciotti, M.V. Mansilla, D. Tobia, M. S. Nadal, T.E. Torres, E. De Biasi, C.A. Ramos, G.F. Goya, R.D. Zysler, E. Lima, Free-radical formation by the peroxidase-like catalytic activity of MFe₂O₄ (M = Fe, Ni, and Mn) nanoparticles, *J. Phys. Chem. C* 123 (2019) 20617–20627.
- [42] D. Bayot, M. Devillers, Peroxo complexes of Niobium(V) and Tantalum(V), *Coord. Chem. Rev.* 250 (2006) 2610–2626.
- [43] R.A. Sheldon, M. Wallau, I.W.C.E. Arends, U. Schuchardt, Heterogeneous catalysts for liquid-phase oxidations: Philosophers' Stones or Trojan Horses? *Acc. Chem. Res.* 31 (1998) 485–493.
- [44] K. Nakajima, Y. Baba, R. Noma, M. Kitano, J.N. Kondo, S. Hayashi, M. Hara, Nb₂O₅•nH₂O as a heterogeneous catalyst with water-tolerant Lewis acid sites, *J. Am. Chem. Soc.* 133 (2011) 4224–4227.